HOKKAIDO UNIVERSITY

Title	Aerodynamic Heating Prediction of an Inflatable Reentry Vehicle in a Hypersonic Wind Tunnel
Author(s)	Matsunaga, Manabu; Takahashi, Yusuke; Oshima, Nobuyuki; Yamada, Kazuhiko
Citation	55th AIAA Aerospace Sciences Meeting https://doi.org/10.2514/6.2017-0263
Issue Date	2017-01
Doc URL	http://hdl.handle.net/2115/71352
Type	proceedings (author version)
File Information	AIAA_Paper_hwt-maac.pdf

Instructions for use

Aerodynamic Heating Prediction of an Inflatable Reentry Vehicle in a Hypersonic Wind Tunnel

Manabu Matsunaga[1], Yusuke Takahashi[2] and Nobuyuki Oshima[3]
Hokkaido University,
Kita 13 Nishi 8, Kita-ku, Sapporo, Hokkaido, 060-8628, Japan,
and
Kazuhiko Yamada[4]
Japan Aerospace Exploration Agency,
3-1-1 Yoshinodai Chuo-ku, Sagamihara, Kanagawa, 252-5210, Japan

Aerodynamic heating around an inflatable reentry vehicle was investigated using hypersonic wind tunnel and numerical approach. The inflatable reentry vehicle is mainly composed of the capsule, membrane aeroshell (rigid in the wind tunnel), and inflatable torus. Basic configuration of the reentry vehicle (HWT-MAAC) is a scaled-down model of SMAAC, which was used in demonstration mission with JAXA / ISAS S-310-41 sounding rocket. Spherical cap of the SMAAC model was replaced by blunt top. Freestream condition of Mach number of 10, reservoir pressure of 2.5 MPa, and reservoir temperature of 950 K was used in the hypersonic wind tunnel test. Heat flux distribution on the surface and density gradient around the HWT-MAAC were measured by infrared thermography and Schliren photograph techniques, respectively. It was found that heat flux distribution widely varies according to angle of attack of the vehicle and a recirculation region near the membrane aeroshell section of the vehicle can appear at high angle of attack. Flow field was also numerically simulated with computational fluid dynamics approach. Analysis solver used here in was RG-FaSTAR, which is a version of JAXA fast aerodynamic routine (FaSTAR). Structures of shock layer and expansion region around HWT-MAAC was discussed through the analysis approach and the wind tunnel results.

Nomenclature

E	=	total energy per unit volume, J/m^3
ns	=	number of species
nm	=	number of molecules
p	=	pressure, Pa
q	=	heat flux, W/m^2
R	=	gas constant, J/(kg$\cdot$K)
t	=	time, s
T	=	temperature, K
u	=	velocity, m/s
u_τ	=	friction velocity, m/s
x	=	coordinate, m
y	=	distance from wall surface, m
y^+	=	non-dimensional distance
Θ	=	characteristic temperature, K
λ	=	thermal conductivity, W/(m$\cdot$K)

---

[1] Graduation student, School of Engineering.
[2] Assistant Professor, Faculty of Engineering.
[3] Professor, Faculty of Engineering.
[4] Assistant Professor, Institute of Space and Astronautical Science.

μ	=	viscosity, m^2/s
υ	=	kinetic viscosity, $Pa \cdot s$
ρ	=	density, kg/m^3
τ	=	stress tensor, Pa

Subscripts
| s | = | species |
| w | = | wall |

I. Introduction

A reentry vehicle with a membrane aeroshell deployable by an inflatable torus structure (inflatable reentry vehicle) is a candidate for a next generation space transport system. The main feature of note for this kind of vehicle, which was originally proposed in the 1960s, is reduction in aerodynamic heating by low ballistic coefficient during atmospheric reentry. In other words, the use of a deployable aeroshell allows the vehicle to be decelerated at a higher altitude. So far, several studies and demonstration flights have been performed by the National Aeronautics and Space Administration (NASA), the European Space Technology (ESA), and the Japan Aerospace Exploration Agency (JAXA). For flare-type thin-membrane aeroshell, several studies of elemental technologies and demonstration flight have been performed as part of the Membrane Aeroshell for Atmospheric-entry Capsule (MAAC) project by several universities and JAXA.

This type of inflatable reentry vehicle as a capsule with a tightly packed aeroshell, e.g., a slender cylindrical shape, is first transported to a given orbit. The vehicle rapidly expands the membrane aeroshell with inflation of the torus tube under vacuum and microgravity conditions on the orbit. The flare-type membrane aeroshell is sustained by the inflatable torus. The vehicle starts to re-enter as being kicked into an atmospheric reentry orbit. Because of the large area and light weight of the aeroshell, the vehicle can achieve a low-ballistic-coefficient flight during atmospheric reentry. Additionally, because the aeroshell deployment is accomplished before deorbit, a critical operation, such as parachute extraction, is possibly dispensed in exchange for the use of the inflatable vehicle during the EDL approach.

Free flight tests for flare-type thin-membrane aeroshell using a scientific balloon were performed in 2004 and 2009.[1,2] The structural strength of a membrane aeroshell was examined using JAXA's low-speed wind tunnel.[3] Because the plasma behind the shock wave becomes weak due to the low-ballistic-coefficient flight, the possibility of vehicle-to-ground-station communication increases compared with a conventional capsule. In Ref.,[4,5] the behavior of the electromagnetic waves around the vehicle during atmospheric reentry was numerically investigated, and the reduction or avoidance of radio frequency (RF) blackout was indicated. Important milestones in the MAAC project include a reentry demonstration using a sounding rocket[6] and atmospheric reentry mission from a Low Earth orbit (TITANS). A reentry demonstration of the SMAAC deployable vehicle was successfully performed using a JAXA/ISAS S-310-41 sounding rocket.[7-10]

For the development of an inflatable vehicle, it is important to evaluate the measured temperature and understand the aerodynamic heating environment of the vehicle during atmospheric reentry. Compared with conventional reentry capsules, an inflatable vehicle is larger, and the membrane aeroshell is deformed by the aerodynamic force. Hence, it is difficult to clarify the thermal behavior of the vehicle with membrane deformation during aerodynamic heating. Computational fluid dynamics (CFD) technique is one of the very effective tools to investigate flow field in detail. So far, aerodynamic heating around SMAAC has been investigated using measurement results by thermocouples and CFD technique by Takahashi et al.[10] Using an unstuctured grid solver, aerodynamics of this kind of the vehicle have also been investigated.[11] However, validation of analysis model for aerodynamic heating prediction is necessarily not sufficient in regions of hypersonic flow and reentry velocity from the low Earth orbit. Recently, hypersonic wind tunnel tests were performed for the inflatable reentry vehicle. The experimental results can be effective candidates to validate a numerical analysis model for reproducing of hypersonic flow. In the present paper, we focus on prediction performance of aerodynamic heating in hypersonic flow and validation of its analysis model.

American Institute of Aeronautics and Astronautics

III. Hypersonic Wind Tunnel Test

A. Wind Tunnel Model: HWT-MAAC

In this study, a model of the inflatable reentry vehicle used in hypersonic wind tunnel tests is called HWT-MAAC. Its configuration is shown in Fig. 1. Note that all dimensions are in unit of millimeters. A blant-body capsule of nose radius of 28.25 mm is used in HWT-MAAC. Diameter of the model is 150 mm. Membrane aeroshell is deformed by aerodynamic force during flight. Thus its shape of HWT-MAAC is determined using a computed result of a membrane deformation model based on a particle method.[12] Rear surface is flat shape. HWT-MAAC is composed of a kind of polyimide plastics: Vespel.[13] Since emissivity of the material is known (ε =0.876),[14] heat flux distribution on surface of HWT-MAAC is measured using radiation equilibrium assumption. In addition, density gradient distribution of shock wave around the model is measured using the Schlieren photograph technique.
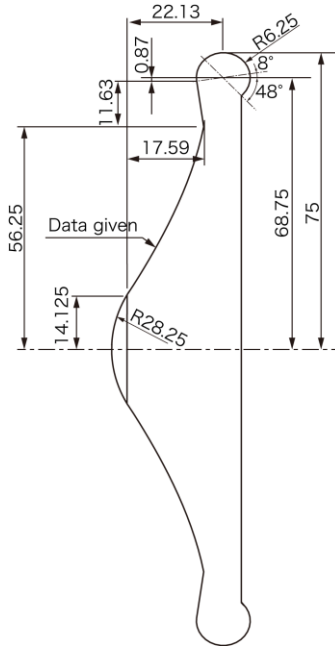
Figure 1. Configrations of HWT-MAAC (all dimensions in mm)

B. Hypersonic Nozzle Flow

Reservoir condition in this wind tunnel test is single as shown in Table 1. Air is used as a test gas. Through a nozzle, the gas supplied by the reservoir tank chocks, and then, is expanded to Mach number of 10 at the nozzle exit. It was reported by Nagata et al.[9] that the inflatable reentry vehicle reenters with high angle of attack at high Mach number altitude in the SMAAC mission. Because aerodynamic force is generally low at high altitude where density is low and Mach number is high before deceleration, it is difficult to rapidly stabilize initial attitude of the vehicle. Thus, it is worth to investigate flow behavior around the vehicle with angle of attack for high Mach number condition. Freestream conditions of five cases and angle of attack (AOA) are listed in Table 2. These flow parameters are determined by the isotropic process in laval nozzle with the reservoir condition and the Mach number at nozzle exit (M = 10). When characteristic length of HWT-SMAAC is 150 mm and viscosity of the freestream is given as 2.83×10^{-3} Pa·s using the Sutherland law, freestream Reynolds number is given by 3.32×10^5.

Table 1. Reservoir condition

Reservoir pressure, Pa	Reservoir temperature, K	Duration time, s
2.5	950	4

Table 2. Freestream conditions

Run number	Velocity, m/s	Density, kg/m^3	Temperature, K	AOA, degree
case1	1346	4.66×10^{-3}	45	0
case2	1346	4.66×10^{-3}	45	10
case3	1346	4.66×10^{-3}	45	20
case4	1346	4.66×10^{-3}	45	30
case5	1346	4.66×10^{-3}	45	40

C. Schlieren Photograph

Density gradient distributions around HWT-MAAC with angle of attack of 0 and 20 degrees are shown in Figs. 2(a) and 2(b), respectively, which are obtained using the Schlieren photograph technique. It is clearly confirmed that strong shock waves appear in front of HWT-MAAC. For the case of AOA of 0 degree, each shock stand-off distance from the capsule, aeroshell, and inflatable torus parts is almost similar. On the other hand, the distance is long on the lower side of the inflatable torus, while that on the upper side is short for the case of AOA of 20 degree. Because heat flux is generally proportion to temperature gradient, heat flux becomes high on the upper side of the torus where the temperature gradient is high, while that becomes low on the lower side.
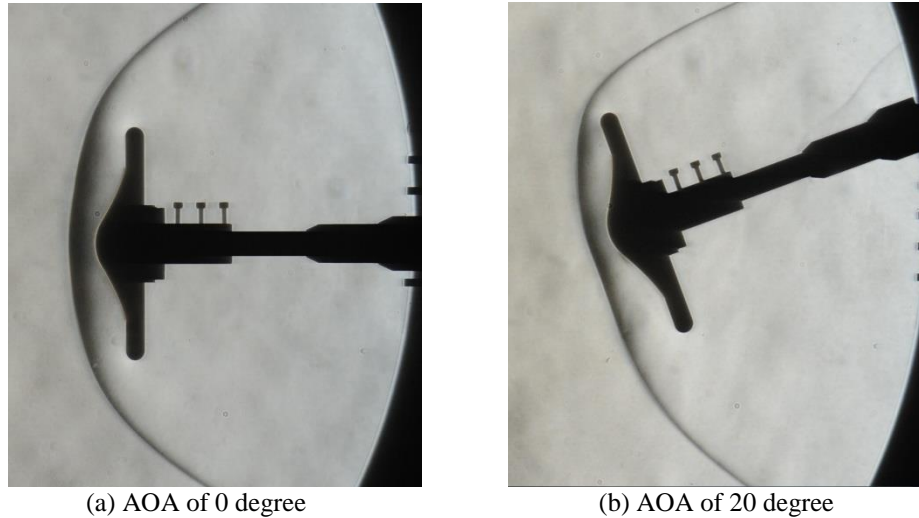

(a) AOA of 0 degree   (b) AOA of 20 degree

Figure 2. Density gradient distribution around HWT-MAAC by Schieren photograph technique for case1 and case3

D. Infrared Thermograph

Figures 3(a) and 3(b) show heat flux distributions on the surface of HWT-MAAC with angle of attack of 0 and 20 degrees, respectively. Note that unit in the heat flux in the figure is kW/m^2. These heat fluxes are obtained using the infrared camera assuming radiation equilibrium on the surface using known emissivity of the polyimide plastic. For the case of AOA of 0 degree, heat flux reaches the peak value of approximately 90 kW/m^2 on the top of capsule part, while heat flux on the inflatable torus is approximately 70 kW/m^2. On the aeroshell surface, heat flux varies from 60 kW/m^2 on the capsule side to 30 kW/m^2 on the torus side. On the other hand, the peak heat flux of approximately 115 kW/m^2 appears on the inflatable torus for the case of AOA of 20 degree. This is mainly because the shock stand-off distance becomes short near the torus decrease with an angle of attack, and then, temperature

gradient on the surface becomes high. It is confirmed that heat flux decreases on the sides of lower torus and aeroshell because the shock stand-off distance increases as discussed above (see also 2(b)). Flow in the shock layer is expected to separate on the top of capsule, and then, attaches on these regions forming recirculation region near the aeroshell surface, when HWT-SMAAC has certain angle of attack.
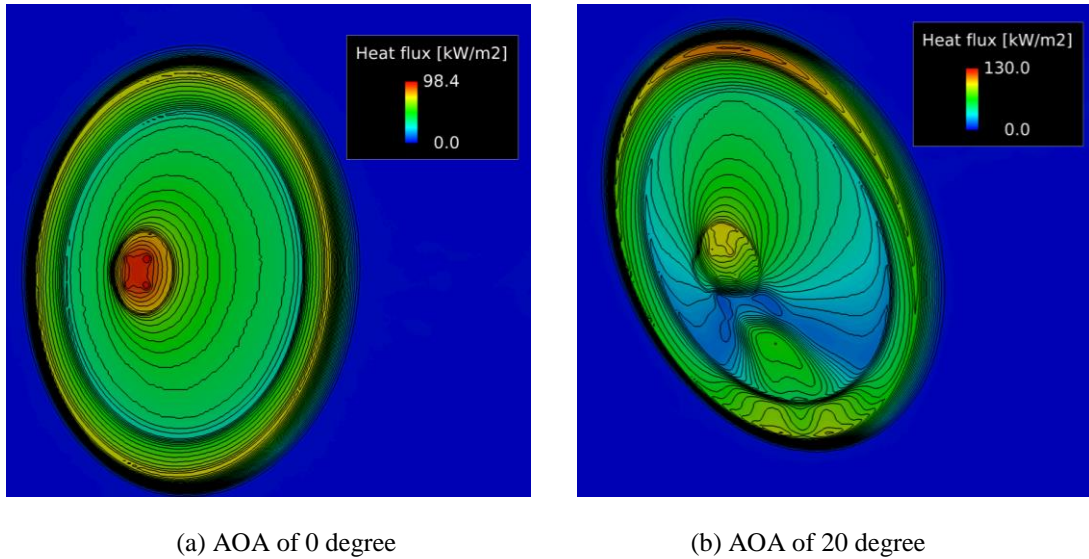

(a) AOA of 0 degree   (b) AOA of 20 degree

Figure 3. Heat flux distribution on HWT-MAAC surface measured by thermography technique for case 1 and case 3 (dimension in kW/m^2).

III. Formulations

A. Analysis Object

Computational model of HWT-MAAC is shown in Fig. 4. The model is constructed based on CAD (computer-aided design) data of the wind tunnel model. However, sting to support the model attaching the balance and wind tunnel facility is not reproduce. It was reported by Ha et al.[11] that effect of wake flow for this kind of reentry vehicle is relatively small for hypersonic flow region. It is not important to reproduce sting in this analysis.

(a) Front side view   (b) Rear side view
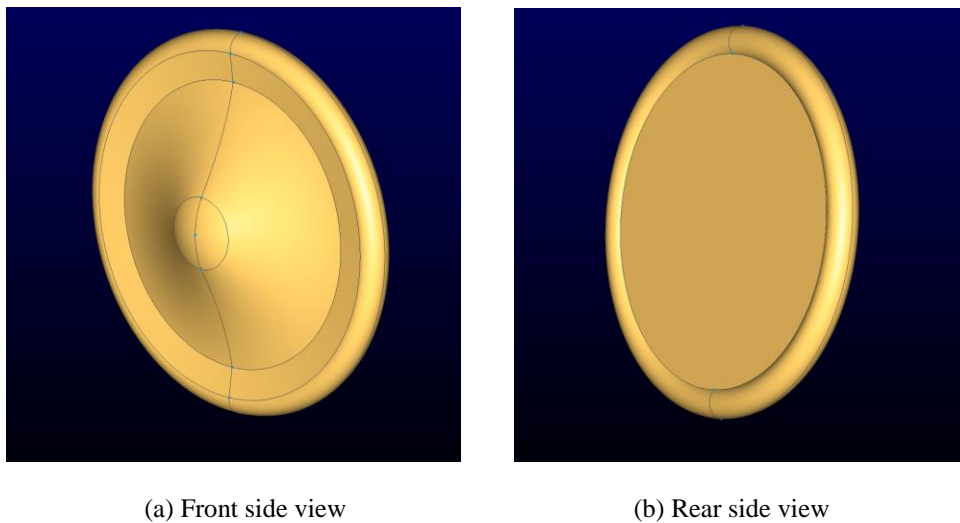
Figure 4. Analysis model of HWT-MAAC

B. Flow Field Model

First of all, the following assumptions are employed here: (1) The flow is continuum and lamiar; (2) The gas considered is air which is composed of 0.765 of N_2 and 0.235 of O_2 in mass fraction; (3) No chemical reaction occurs.

The flow field is described by the Navier-Stokes equations and the equation of state. The equations are composed of the total mass, momentum, and total energy conservations, which can be expressed as follows:

$$\frac{\partial \rho}{\partial t} + \frac{\partial}{\partial x_j}\left(\rho u_j\right) = 0, \tag{1}$$

$$\frac{\partial \left(\rho u_j\right)}{\partial t} + \frac{\partial}{\partial x_j}\left(\rho u_i u_j + \delta_{ij} p\right) = \frac{\partial \tau_{ij}}{\partial x_j}, \tag{2}$$

$$\frac{\partial E}{\partial t} + \frac{\partial}{\partial x_j}\left[(E + p)u_j\right] = \frac{\partial}{\partial x_j}\left(u_j \tau_{ij} + q_j\right), \tag{3}$$

where δ_{ij} is the Kronecker's delta. Furthermore, τ_{ij} and q_j are the stress tensor and heat flux, which are, respectively, given by

$$\tau_{ij} = \mu\left(\frac{\partial u_i}{\partial x_j} + \frac{\partial u_j}{\partial x_i} - \frac{2}{3}\frac{\partial u_k}{\partial x_k}\delta_{ij}\right), \tag{4}$$

$$q_j = \lambda\frac{\partial T}{\partial x_j}. \tag{5}$$

The equation of state can be expressed as

$$p = \sum_{s=1}^{ns} \rho_s R_s T. \tag{6}$$

The total energy E is given by

$$E = \sum_{s=1}^{ns} \frac{5}{2}\rho_s R_s T + \sum_{s=1}^{nm} \frac{\rho_s R_s \Theta_{vib,s}}{\exp\left(\Theta_{vib,s}/T\right)} + \frac{1}{2}\rho u_j u_j, \tag{7}$$

where $\Theta_{vib,s}$ is the vibrational characteristic temperature. Transport properties, such as molecular viscosity, thermal conductivity and diffusion coefficients are evaluated by the Gupta model, which is based on the first Chapman-Enskog approximation[15].

C. Software Package: RG-FaSTAR

In the present study, RG-FaSTAR v2.0.0[16] is adopted. RG-FaSTAR is a high-enthalpy flow solver that incorporates real gas effects and thermochemical nonequilibrium, and is a version of the fast unstructured CFD code "FaSTAR",[17] originally developed by JAXA. This solver can handle unstructured grid systems including tetrahedral, triangular prism, square pyramid, and hexahedral meshes, and have high flexibility in generating the computational grid. For massive parallel computation on a high-performance computer, the message passing interface (MPI) technique with a domain partition approach is adopted.

The governing equations of the flow field are solved using a finite volume approach. All the flow properties are set at the center of a control volume. The advection fluxes in the NS equations are calculated using the SLAU scheme with the MUSCL interpolation method for high accuracy. On the other hand, the viscous fluxes are evaluated using the second-order central difference method. The spatial gradients of the flow properties are calculated using the weighted Green-Gauss method. Time integration is performed using an implicit time-marching method. The governing equation system is transformed into the delta form, and the solution is updated at each time step.

D. Calculation Conditions

Computational domain and boundary condition for HWT-MAAC computations are shown in Fig. 5. As boundary conditions, freestream conditions listed in Table 2 are given on the inlet boundary. On the outlet boundary, zeroth extrapolation is imposed. Non slip for the velocity, fixed temperature of 150 K, no pressure gradient normal to the wall are assumed on the wall.
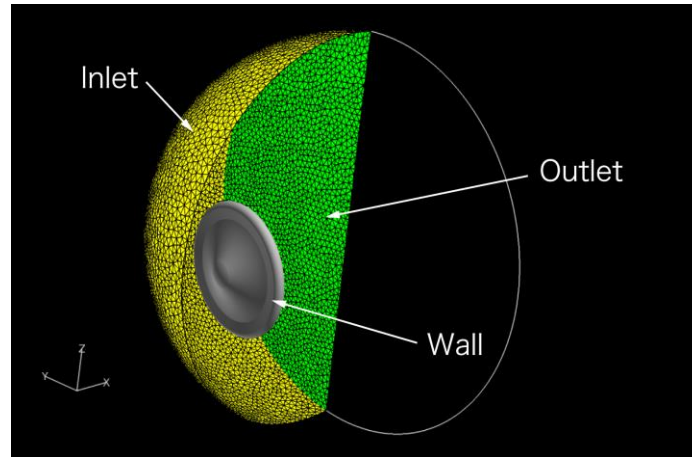

Figure 5. Computational domain and boundary conditions for HWT-MAAC analysis

Figure 6 is illustration of computational grids for HWT-MAAC analysis. By using the non-structural grids, human cost to generate computational mesh may drastically reduce, compared with grid generation by structural grids such as all hexahedral meshes. Most of the meshes in the computational domain is composed of tetrahedral mesh. Prism mesh to solve boundary layer near the wall is partly generated. To resolve sharply shock wave in front of the vehicle, very fine prism mesh is used. Pointwise/Gridgen is used to generate the grids. Number of cells and nodes of computational grids are approximately 20,500,000 and 7,460,000.
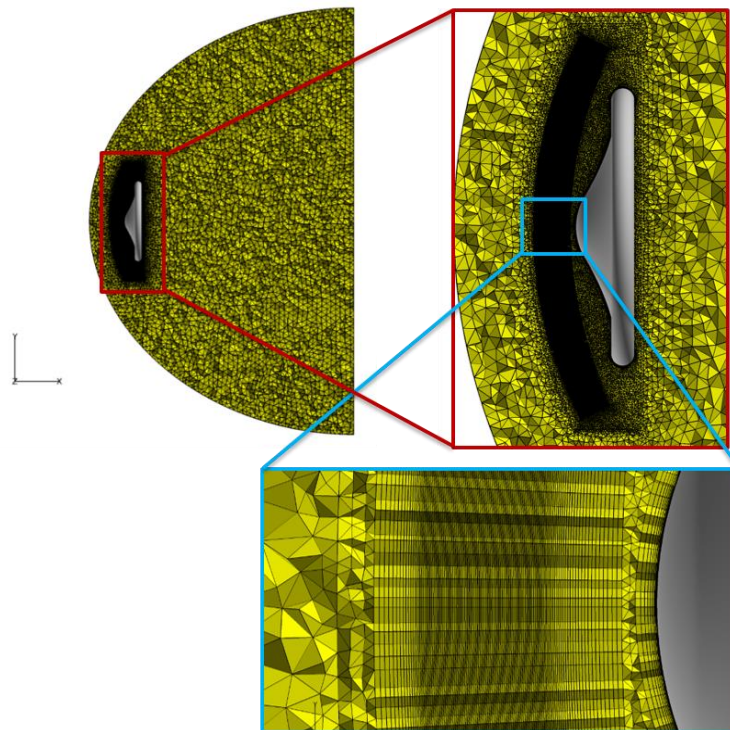
Figure 6. Computational grids for HWT-MAAC analysis

7

American Institute of Aeronautics and Astronautics

IV. Result and Discussion

A. Density Gradient Distribution

As shown in Figs. 2, which are experimental results by the Schlieren photograph technique, a strong shock wave is formed in front of HWT-MAAC. In addition, an expansion region in the rear region is also formed. Compared with shock layer in front of the model, aerodynamic heating in the rear region does not necessarily becomes a critical problem, because air density reduces and gas temperature is relatively low behind the model. Thus, we mainly focus on front shock layer in this study.

In the present numerical analysis, density gradient in x direction is evaluated as follows:

$$Grad(\rho).x = \frac{\partial \rho}{\partial x}. \tag{8}$$

Figure 7 (a) and 8 (a) show distributions of density gradient in x direction around HWT-MAAC at AOA of 0 and 20 degrees. Density gradients become high along the shock wave. These distributions are similar with the Schlieren photographs. Moreover, high gradients of density appear near the HWT-MAAC surface, because air density becomes high with decrease in temperature. Figure 7 (b) and 8(b) show comparisons of the density gradient in x direction around HWT-MAAC between the experiment and numerical simulation at each AOA. In these figures, computed density gradients are overlapped on the Schlieren photographs. The overlapped distributions show good agreements. It is indicated that the present analysis model reproduced shock stand-off distance around HWT-MAAC at AOA of 0 and 20 degrees.
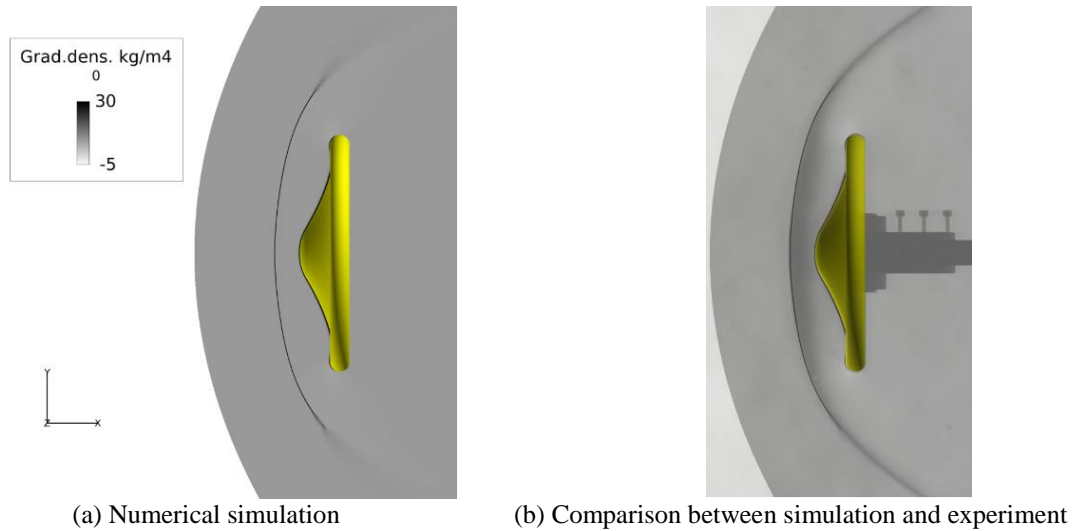

(a) Numerical simulation   (b) Comparison between simulation and experiment

Figure 7. Density gradient distribution around HWT-MAAC at AOA of 0 degree

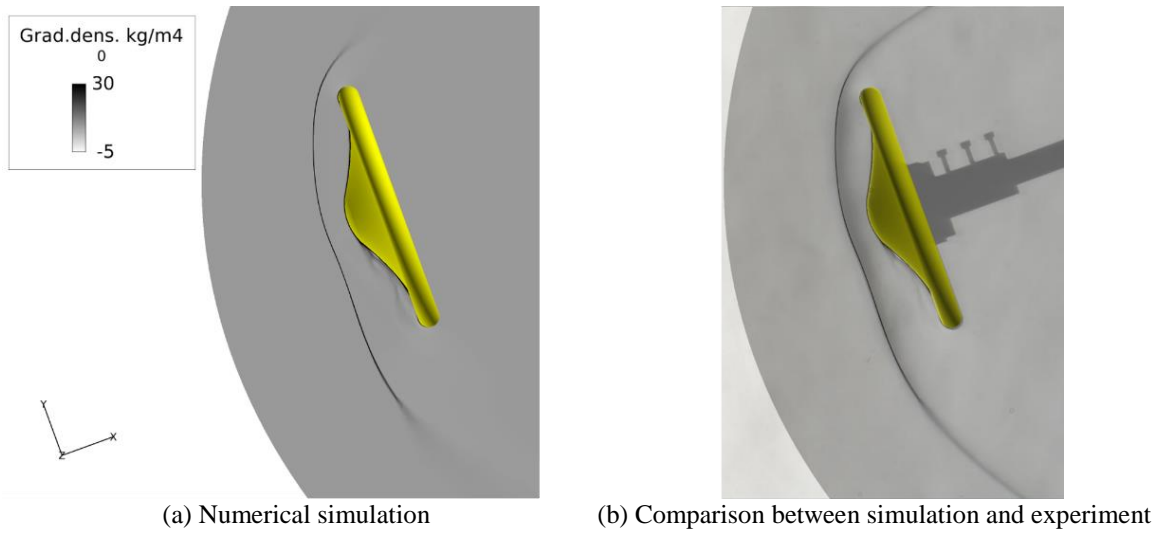(a) Numerical simulation   (b) Comparison between simulation and experiment

Figure 8. Density gradient distribution around HWT-MAAC at AOA of 20 degree

B. Flow Field behind Shock Wave

Figures 9, 10, and 11 show computational results of pressure, gas temperature, and Mach number around HWT-MAAC at AOA of 0 degree, respectively. Peak pressure and temperature in the shock layer are approximately 7800 Pa and 910 K, respectively. These flow variables are almost uniform near each of the capsule and aeroshell in the shock layer. On the other hand, pressure and temperature decrease near the inflatable torus, because compressed gas in the shock layer passes near the torus and inflows in the rear with strong expansion. It is confirmed in Fig. 11 that the Mach number rapidly increases near the torus. A ring-shape vortex is generated in the wake region. Temperature increases somewhat in the wake due to exchange mechanism of internal energies between kinetic energy and thermal energy. However, since air density is low, aerodynamic heating is never strong on the rear surface.
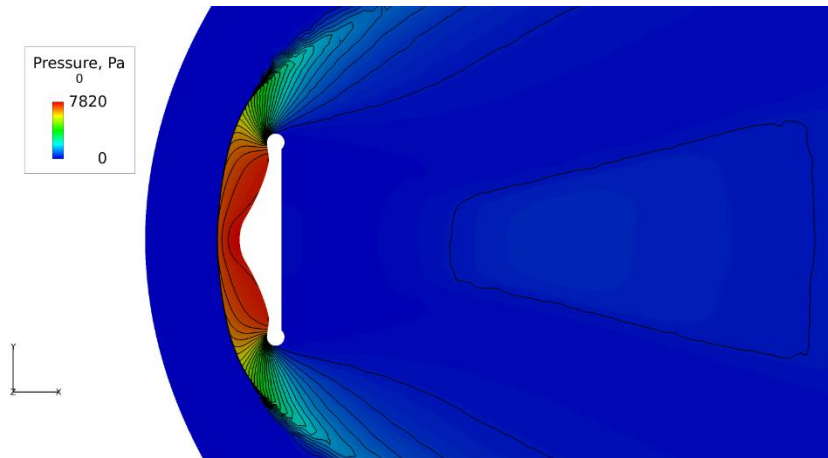
Figure 9. Pressure distribution around HWT-MAAC at AOA of 0 degree.
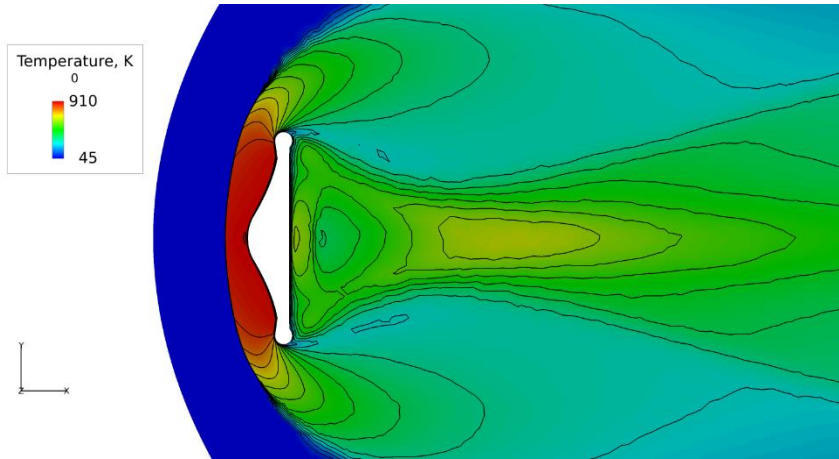
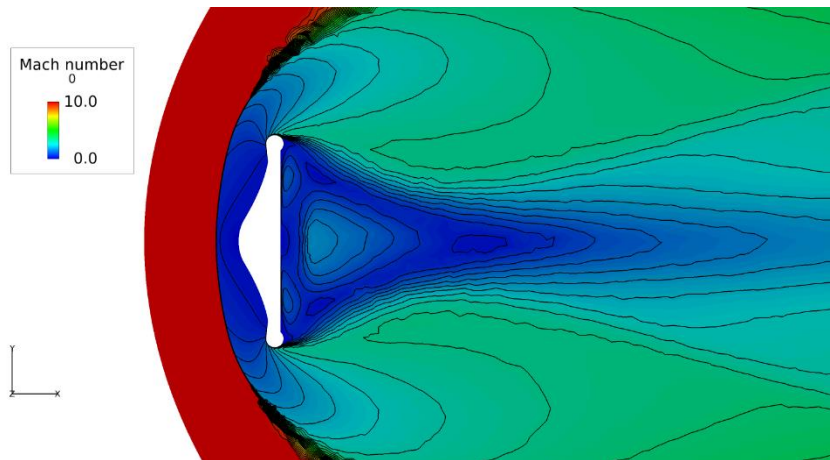Figure 10. Gas temperature distribution around HWT-MAAC at AOA of 0 degree.

Figure 11. Mach number distribution around HWT-MAAC at AOA of 0 degree.

Figures 12, 13, and 14 show numerical results of pressure, gas temperature, and Mach number around HWT-MAAC at AOA of 20 degree, respectively. Peak pressure and temperature in the shock layer are almost the same as the case for AOA of 0 degree. However, these flow variables are lower at the lower side of the aeroshell. In addition, a recirculation region in low temperature appears on the lower side surface. Pressure and temperature sharply decrease near the upper inflatable torus, because the test gas is compressed more strongly at the upper aeroshell and inflows in the rear with strong expansion. It is confirmed in Fig. 14 that the Mach number more rapidly increases near the upper inflatable torus. A ring-shape vortex shown in the case of AOA of 0 degree is broken in the wake region at AOA of 20 degree. Effect of AOA for aerodynamic heating on the rear surface seems to be low.
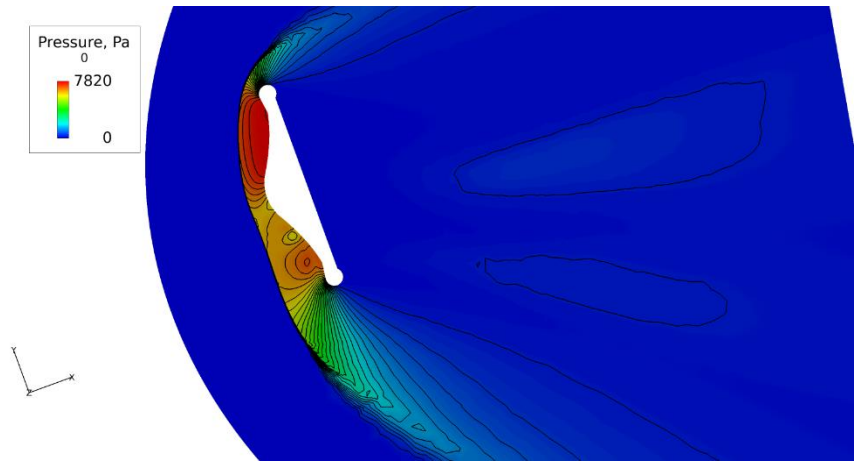
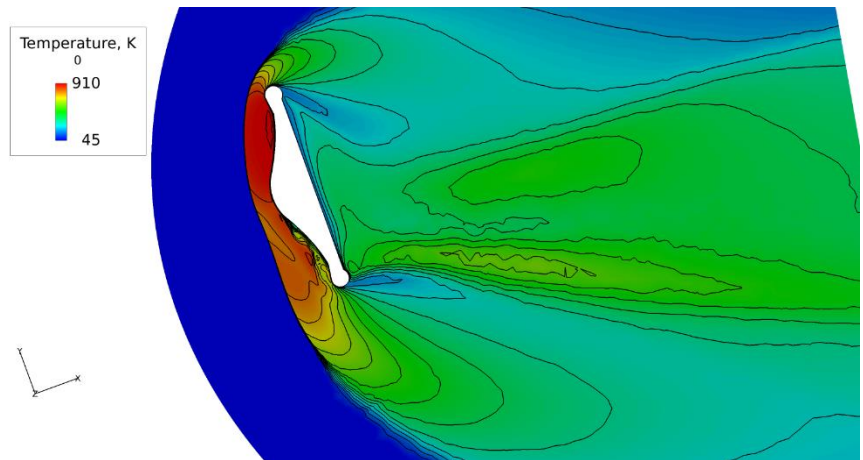Figure 12. Pressure distribution around HWT-MAAC at AOA of 20 degree.

Figure 13. Gas temperature distribution around HWT-MAAC at AOA of 20 degree.
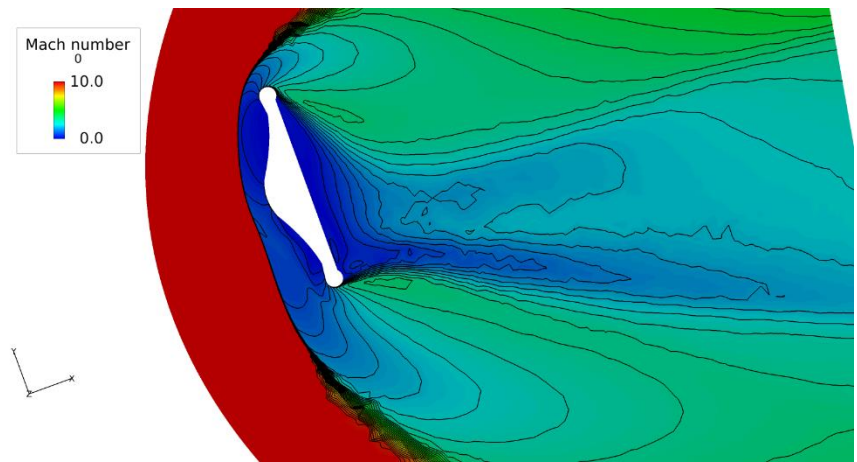

Figure 14. Mach number distribution around HWT-MAAC at AOA of 20 degree.

C. Heat Flux Distribution

Heat flux on the HWT-SMAAC surface is given by

$$q = \lambda \frac{\partial T}{\partial n}\bigg|_0 ,$$

(9)

where λ and $\partial T / \partial n\big|_0$ are the thermal conductivity and temperature gradient between the boundary cell and its neighboring cell. A non-dimension distance, y^+, can be expressed as follows:

$$y^+ = \frac{u_\tau y}{\upsilon} ,$$

(10)

where y shows distance from wall surface and υ is the kinetic viscosity, respectively. In addition, the friction velocity, u_τ, is given by

$$u_\tau = \sqrt{\frac{\tau_w}{\rho}} .$$

(11)

Since the non-dimension distance on the HWT-SMAAC surface, y^+, is within 2.1, the distance is expected to be sufficiently small in order to calculate heat flux on the surface.

Figure 15 shows computational result of a heat flux distribution on front surface of HWT-MAAC at AOA of 0 degree. Concentric distribution of the heat flux is confirmed on the surface. Peak heat flux is on the capsule surface. Figure 16 shows comparison of heat flux on front surface at AOA of 0 degree between experiment and numerical simulation. Shape of HWT-MAAC is also described. For the presently-used measurement system of heat flux with the infrared thermography, it was reported that error of approximately ± 10 % appears.[14] Simulation result shows very good agreement with experiment data. It is indicated that the present analysis model reproduces heat flux on front surface of HWT-MAAC.
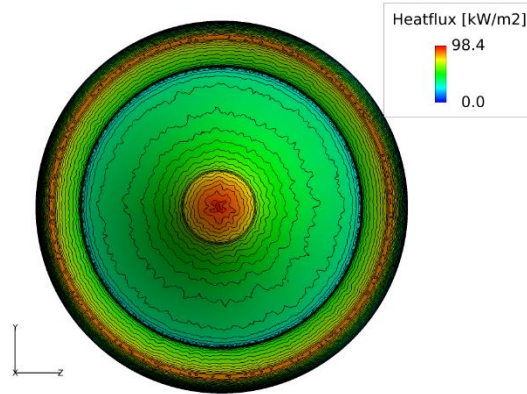

Figure 15. Heat flux distribution on front surface of HWT-MAAC at AOA of 0 degree
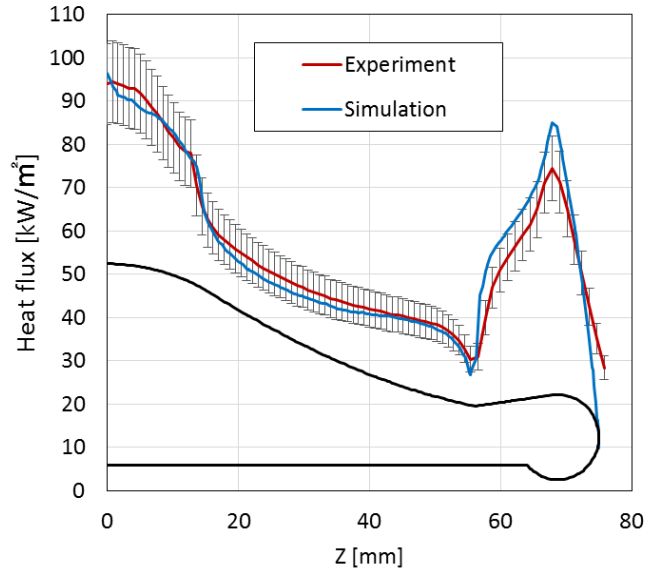
Figure 16. Comparison of heat flux on front surface of HWT-MAAC at AOA of 0 degree between experiment and numerical analysis.

Figure 17 shows numerical result of heat flux distribution on front surface of HWT-MAAC at AOA of 20 degree. Heat flux is higher at upper sides of capsule and inflatable torus. Peak heat flux appears at the upper of inflatable torus. On the other hand, heat flux decreases on the lower side of the aeroshell. These distributions are almost the same as experiment. However, heat flux distribution in center on the lower side of the aeroshell is different between the experiment and the numerical simulation. Laminar flow assumption is used in the present analysis model. Considering that the Reynolds number is 3.32×10^5 for the case, it is possible that the flow field partly or totally becomes turbulent. Heat flux generally becomes high when considering turbulence. Introduction of a turbulence model may be required as a future work.

 Figure 18 shows computational result of stream lines around HWT-MAAC at AOA of 20 degree. The flow separates on the capsule. In addition, vortexes are generated after the separation. Figure 19 shows numerical result of stream lines and heat flux distribution on front surface of HWT-MAAC at AOA of 20 degree. It is confirmed that the vortexes appear on the lower heat flux region. The vortexes strongly affect the heat flux distribution on the front surface. It should be noted that the flow field after separation can change by considering turbulence. For detail investigation of aerodynamic heating with AOA, reproduction of vortex behavior is a key issue.
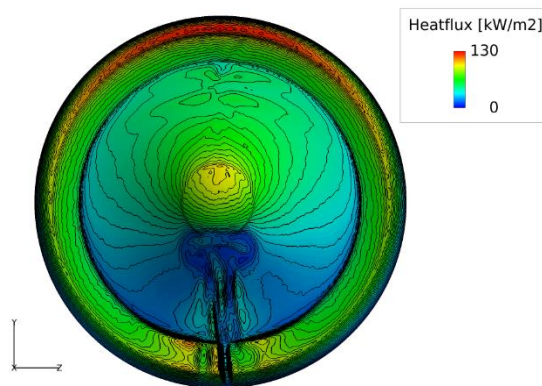

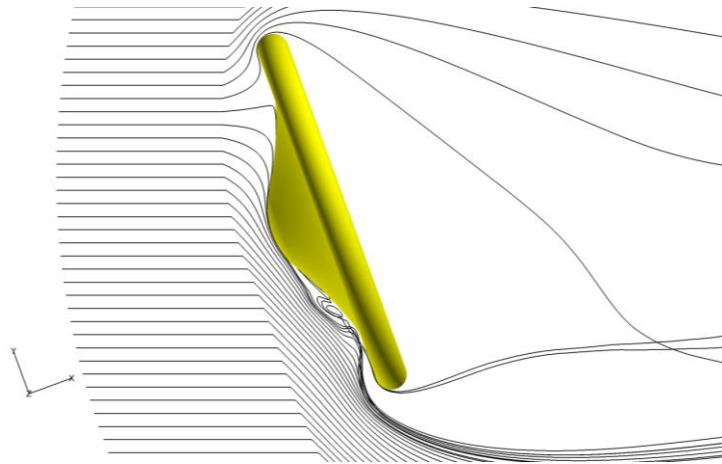Figure 17. Heat flux distribution on front surface of HWT-MAAC at AOA of 20 degree

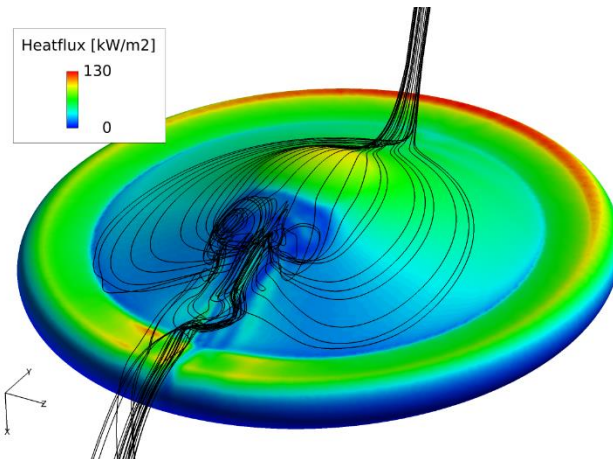Figure 18. Stream lines around HWT-MAAC at AOA of 20 degree.

Figure 19. Stream lines and heat flux distribution on front surface of HWT-MAAC at AOA of 20 degree.

V. Conclusion

Aerodynamic heating in a hypersonic wind tunnel around a thin-membrane flare-type inflatable reentry vehicle (HWT-MAAC) was numerically and experimentally investigated. For analysis model, in order to generate computational grids in the present analysis model with reduction of human cost, unstructured grids system was adopted. As applicable solver to this type of grid system, FaSTAR/RG-FaSTAR was used. In the hypersonic wind tunnel tests, density gradient distributions around the HWT-MAAC and heat fluxes on the surface of the model were obtained with the Schieren photograph and infrared thermography techniques, respectively. These variables distributions are compared with the computed results, and then, validation of the analysis model was performed. The analysis model well reproduced the shock layer and aerodynamic heating without AOA of 0 degree. Flow behavior in the shock layer was cleared without AOA case. On the other hand, at AOA of 20 degree, it is found that flow separates on the capsule and a recirculation region is formed in the shock layer. Heat flux on the membrane surface in the recirculation was slightly different between the experiment and numerical simulation. Since the Reynolds number is 3.32×10^5, the flow field was turbulent. For more accurate investigation of flow field behavior with AOA case, consideration of a turbulence effect need to be introduced to the analysis model.

Acknowledgments

References

[1]K. Yamada, D. Akita, E. Sato, K. Suzuki, T. Narumi, and T. Abe. "Flare-Type Membrane Aeroshell Flight Test at Free Drop from a Balloon". *Journal of Spacecraft and Rockets*, 46(3):606-614, May-June 2009.

[2]K. Yamada, T. Abe, K. Suzuki, N. Honma, M. Koyama, Y. Nagata, D. Abe, Y. Kimura, A.K. Hayashi, D. Akita, and H. Makino. "Deployment and Flight Test of Inatable Membrane Aeroshell using Large Scienti_c Balloon". *AIAA Paper 2011-2579*, 2011.

[3]K. Yamada, T. Sonoda, K. Nakashino, and T. Abe. "Structural Strength of Flare-type Membrane Aeroshell Supported by Inflatable Tours against Aerodynamic Force". In *Proceedings of 28th International Symposium on Space Technology and Science*, ISTS 2011-c-34, Okinawa, Japan, June 5 - 12 2011.

[4]Y. Takahashi, K. Yamada, and T. Abe. "Radio Frequency Blackout Possibility for an Inatable Reentry Vehicle". *AIAA Paper 2012-3110*, 2012.

[5]Y. Takahashi, K. Yamada, and T. Abe. "Examination of Radio Frequency Blackout for an Inatable Vehicle during Atmospheric Reentry". *Journal of Spacecraft and Rockets*, 51(2):430-441, March 2014.

[6]K. Yamada, T. Abe, K. Suzuki, O. Imamura, and D. Akita. "Reentry Demonstration Plan of Flare-type Membrane Aeroshell for Atmospheric Entry Vehicle using a Sounding Rocket". *AIAA Paper 2011-2521*, 2011.

[7]K. Yamada, Y. Nagata, N. Honma, D. Akita, O. Imamura, T. Abe, and K. Suzuki. "Reentry Demonstration Deployable and Flexible Aeroshell for Atmospheric-Entry Vehicle using Sounding Rocket". In *Proceedings of 63th International Astronau-tical Congress*, AC-12-D2.3.3, Naples, Italy, October 1 - 5 2012.

[8]K. Yamada, Y. Nagata, T. Abe, K. Suzuki, O. Imamura, and D. Akita. "Reentry Demonstration of Flare-type Membrane Aeroshell for Atmospheric Entry Vehicle using a Sounding Rocket". *AIAA Paper 2013-1388*, 2013.

[9]Y. Nagata, K. Yamada, T. Abe, and k Suzuki. "Attitude Dynamics for Flare-type Membrane Aeroshell Capsule in Reentry Flight Experiment". *AIAA Paper 2013-1285*, 2013.

[10]Y. Takahashi, K. Yamada, T. Abe, and K. Suzuki. "Aerodynamic Heating around Flare-type Membrane Inatable Vehicle in Suborbital Reentry Demonstration Flight". *Journal of Spacecraft and Rockets*, 52(6):1530-1541, Novermber 2015.

[11]D. HA, Y. TAKAHASHI, K. YAMADA, and T. ABE. "Aerodynamic Simulation of Inatable Re-Entry Vehicle Performance in Low Speed Wind Tunnel". *TRANSACTIONS OF THE JAPAN SOCIETY FOR AERONAUTICAL AND SPACE SCIENCES, AEROSPACE TECHNOLOGY JAPAN*, 12(ists29):Po 2 57-Po 2 62, 2014.

[12]K. Yamada, Y. Kato, and T. Abe. "Numerical Simulation of Hypersonic Flow around Flare-Type Aeroshell with Torus Frame". In *Proceedings of 6th Asia Workshop on Computational Fluid Dynamics*, Kashiwa, Japan, March 16 2009.

[13]Du Pont. "Vespel technical data". http://www.dupont.com/products-and-services/plastics-polymers-resins/parts-shapes/brands/vespel-polyimide.html.

[14]T. Koyama, S. Tsuda, N. Hirabayashi, H. Sekine, K. Hozumi, and M.Watari. "Measurement of Heat Transfer Distribution by Infrared Thermography Technology". *JAXA Research and Development Report*, 6:1-30, 2007. (in Japanese).

[15]R. N. Gupta, J. N. Yos, R. A. Thompson, and K. P. Lee. "A review of reaction rates and thermodynamic and transport properties for an 11-species air model for chemical and thermal nonequilibrium calculations to 30000 K". *NASA RP-1232, Aug. 1990.*

[16]Y. Takahashi. "Advanced validation of CFD-FDTD combined method using highly applicable solver for reentry blackout Prediction". *Journal of Physics D: Applied Physics*, 49(1):015201, 2016.

[17]A. Hashimoto, K. Murakami, T. Aoyama, K. Ishiko, M. Hishida, M. Sakashita, and P.R. Lahur. "Toward the Fastest Unstructured CFD". *AIAA Paper 2012-1075*, 2012.